 doi:10.20944/preprints202110.0432.v1

Article

Silver flowerlike structures for surface-enhanced Raman spectroscopy

Gitchka G. Tsutsumanova [1], Neno D. Todorov [1], Stoyan C. Russev[1], Miroslav V. Abrashev[1], Alexey V. Lukoyanov[2,3] and Victor G. Ivanov[1,*]

[1] Sofia University, Faculty of Physics, 5 James Bourchier Blvd., 1164 Sofia, Bulgaria; ggt@phys.uni-sofia.bg (G.G.T.), neno@phys.uni-sofia.bg (N.D.T.), scr@phys.uni-sofia.bg (S.C.R.), mvabr@phys.uni-sofia.bg (M.V.A.)
[2] M.N. Miheev Institute of Metal Physics, Ural Branch, Russian Academy of Sciences, S. Kovalevskaya St., 18, Ekaterinburg, 620108, Russia, lukoyanov@imp.uran.ru (A.V.L.)
[3] Ural Federal University, Mira St., 19, Ekaterinburg, 620002, Russia
* Correspondence: vgi@phys.uni-sofia.bg (V.G.I.)

Abstract: Micro- and nanoflowers are a class of materials composed of particles with high surface-to-volume ratio. They are being extensively studied in the last decade due to simple preparation protocols and promising applications in biosensing, as drug delivery agents, for water purification and so on. Flowerlike objects, due to their highly irregular surface, may act also as plasmonic materials, providing resonant coupling between optical waves and surface plasmon excitations. This fact infers for the possibility to use micro- and nanoflowers as effective surface-enhanced Raman scattering (SERS) substrate materials. Here, we report on the design and Raman enhancement properties of silver flowerlike structures, deposited on aluminum surface. A simple and cost-effective fabrication method is described, which leads to SERS substrates of high developed surface area. The morphology of the silver flowers on a nanoscale is characterized by self-organized quasiperiodic stacks of nanosheets, which act as plasmonic cavity-resonators. The substrates were tested against rhodamine-6G (R6G) water solutions of concentration varying between 10^{-3} M and 10^{-7} M. Optimal SERS enhancement factors of up to 10^5 were established at R6G concentrations in the range 10^{-6} – 10^{-7} M.

Keywords: SERS; SERS substrates; nanoflowers;;surface plasmon; nanocavity resonator

1. Introduction

Surface-enhanced Raman scattering (SERS) is a powerful analytical technique, which undergoes substantial evolution over the years [1–4]. Currently, there is a broad range of SERS applications, among which single molecule detection [5–7], biosensing [8–10], gas detection ("artificial nose") [11], etc. There are two principal mechanisms that lead to SERS effect – the chemical and the electromagnetic (EM) enhancement. The former is a result of adsorbate-substrate bonding interactions resulting in surface electronic states of high Raman polarizability [12]. The EM enhancement stems from resonant coupling between the incident or scattered photons with the surface plasmon (SP) or localized plasmon (LP) excitations on a non-planar metallic surface [13]. Typically, noble metals (silver, gold) are the best candidates for SERS substrate materials since they provide SP/LP resonance frequencies in the visible range in combination with low electromagnetic losses [14].

As a rule, the EM enhancement is not uniform over the substrate, but is localized on specific "hot spots", where local electric field created by SP/LP excitations overwhelms by orders of magnitude the amplitude of the incident light wave. Hot spots are usually formed due to the lightning-rod effect, e.g. in the gap between closely separated nanoparticles [7,15,16], or near sharp metallic tips [17,18] (a SERS clone known as tip-enhanced Raman spectroscopy – TERS) . Since the morphology of the substrate plays

Preprints (www.preprints.org) | NOT PEER-REVIEWED | Posted: 28 October 2021 doi:10.20944/preprints202110.0432.v1

a key role in the EM enhancement, much effort is being paid to the SERS substrate design. Currently, many preparation techniques are being used, like electrochemically roughened surfaces [19,20], deposition of metallic nanoparticles on a dielectric support/substrate [21–26], micrometer sized metallic sheets [27,28], nanoholes [29], nanorods and nanowires [30], etc. A special attention is being paid to periodic nanoscale arrays, since they allow for finer tuning of the SP resonance in a desirable spectral range [31–34].

Yet another important factor in SERS is the effective area of the active surface. Generally, elevated Raman signal could be retrieved from substrates of larger developed area due to the higher number of adsorbed molecules within irradiated surface. In this aspect micro- and nanoflowers (NF) are an interesting new class of materials [35,36]. Typically, the NF is an object composed of several individual sheets (leafs) organized in specific pattern, oftentimes resembling a real flower. Due to the large surface-to-volume ratio, NFs find promising applications in biosensors, catalysis, drug delivery , etc [36]. The highly irregular surface is favorable for effective light-SP/LP coupling and hot spots formation, which infers for NP applications as plasmonic materials and SERS substrates. Recently, ZnO/Ag nanoflower composites has been reported as SERS substrate materials [37] with enhancement factors up to 10^7 and detection levels down to 10^{-12} M. The NFs has been composed of a ZnO base uniformly covered with Ag nanoparticles responsible for the hot spots formation. Typically for the nanoparticle-based SERS substrates, the SERS enhancement has been found localized around isolated hot spots.

The principal aim of the present work was to further investigate the capabilities of metallic flowerlike structures as SERS substrate materials. Our intent was to combine the large surface-to-volume ratio of the NFs with the evenly distributed SERS response characteristic of the artificial periodic nanostructures. Objects of investigation were the earlier reported silver flowers ("roses") deposited on aluminum surface [38], due to the simple chemical route of preparation and the possibility of ordering in 2D arrays. In particular, we were interested on the influence of the nanoscale morphology of the silver roses on their SERS enhancement. As will be shown below, the as prepared silver flowers display self-organized assemblies of silver nanosheets (leafs) with subwavelength periodicity, which infers for an effective SP interaction with the exciting/scattered optical field.

We describe the preparation and characterization of the substrates, as well as the details of SERS measurements in Section 2. The experimental results are reported and discussed in Section 3. The summary and conclusions of our research are formulated in Section 4. Appendix A describes the details of calculation of the dispersion of the propagating SP waves in a periodic assembly of silver nanosheets.

2. Materials and Methods

2.1. Preparation and Characterization of the SERS Substrates

Silver nitrate, ammonia (25%), and glucose monohydrate were supplied from Merck. Aluminum foil (99%, 100 μm thickness) was obtained from Honeywell Riedel-de Haën, and R6G (R4127, dye content 95 %) – from Sigma.

Silver flowerlike structures were grown on aluminum foil via standard silver mirror reaction. The procedure follows that, described in Reference [39]: 2.5 ml ammonia (1.1 mol/l) was added to 10 ml silver nitrate aqueous solution (0.12 mol/l) until the $AgOH/Ag_2O$ precipitate just disappeared. The $Ag(NH_3)_2OH$ solution was then mixed with 15 ml aqueous solution of glucose (0.56 mol/l). The samples were positioned on the bottom of a petri dish with the as prepared solution. After 60 min they were removed from the solution, rinsed with distilled water and dried in air.

During the growth process of the silver flowers, some of the substrates, referred hereafter as "n" series, were kept at room temperature. The other samples, referred as "s" series, were put on a hot plate and kept at constant temperature of 40°C.

The morphology of the as prepared samples was inspected with a scanning electron microscope (LYRA I XMU, Tescan) equipped with an EDX microanalyzer (Quantax, Bruker). Representative electron micrographs of the "n"and "s" substrates are shown in Figure 1 (a) and (b), respectively. The silver flowers grown on both types of substrates

Preprints (www.preprints.org) | NOT PEER-REVIEWED | Posted: 28 October 2021 doi:10.20944/preprints202110.0432.v1

have comparable diameter of about 20 μm, and consist of thin flakes of a thickness down to 20 nm. A number of lone nanosized silver particles are dispersed on the aluminum surface in a proximity to the silver flowers on the "s"-substrates due to the convection in the solution during the growth on the hot plate. For the "n"-substrates almost no isolated silver particles are found around the flowers. Most of the silver flakes within the flowers are organized in quasiperiodic arrays of 10–15 almost parallel vertically standing sheets, as exemplified by the marked areas 1 and 2 in Figure 1 (a) and (b), respectively. The Fourier transform (FT) amplitude patterns of the selected areas of the microscopic images display diffuse but resolvable peaks corresponding to the propagation wavevector **k** of each array, as indicated in Figure 1 (c) and (d),. The corresponding spatial period Λ of a given stack is, therefore:

$$\Lambda = 2\pi/|\mathbf{k}|. \quad (1)$$

The as estimated average period of the arrays is (580±60) nm for the "n" flowers and (390±30) nm for the "s" flowers. Arrays on the "s"-flowers display better spatial coherence than the arrays formed on the "n"-flowers, as evidenced by Figure 1 (e), where the peaks corresponding to the second and the third overtone of the propagating vector **k** are clearly resolvable. The SEM images allow also estimating the filling factor F of the arrays, i.e. the volume fraction of the silver sheets, which is approximately 0.15 for both types of silver flowers. Thus, the average thickness $b = F\Lambda$ of the silver sheets is about 87 nm for the "n"-flowers and 59 nm for the "s"-flowers.

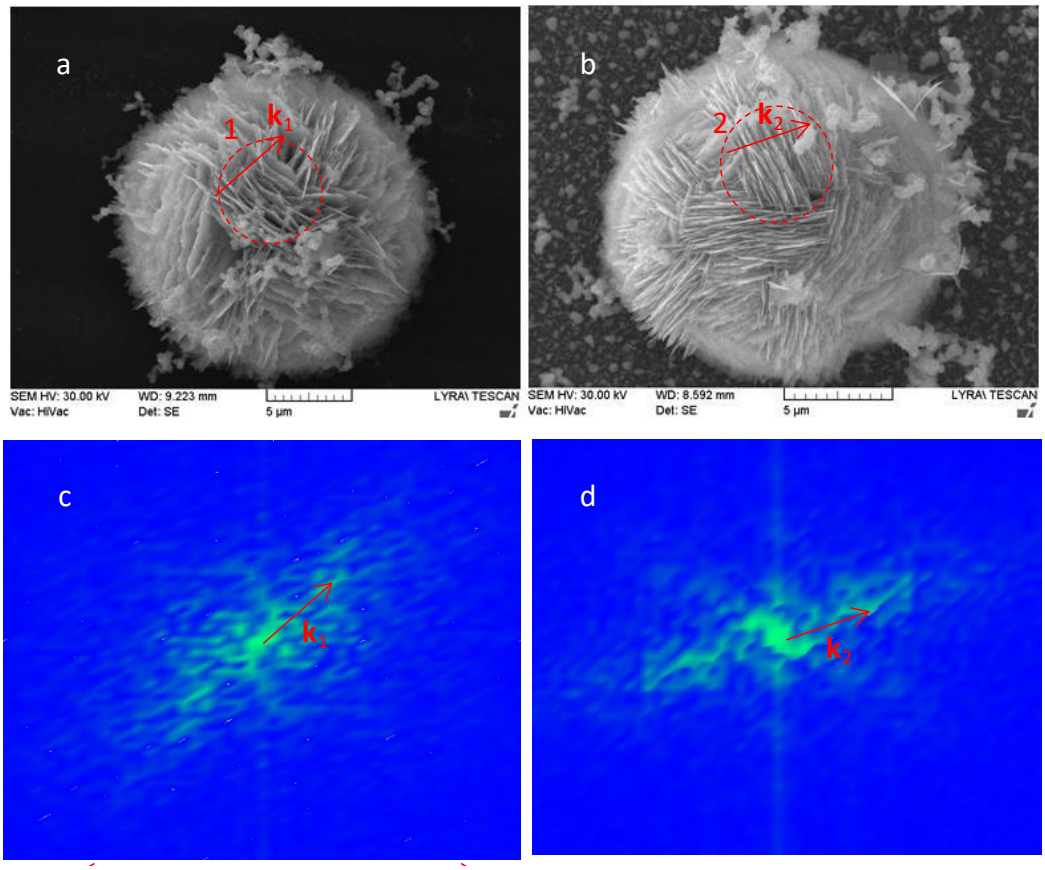

Preprints (www.preprints.org) | NOT PEER-REVIEWED | Posted: 28 October 2021 doi:10.20944/preprints202110.0432.v1

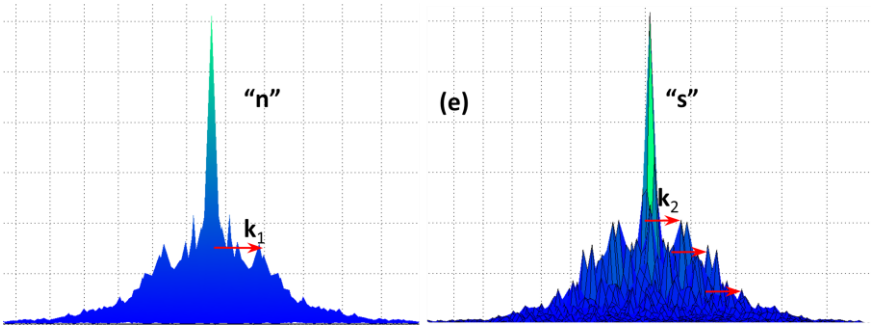

Figure 1. Scanning electron micrographs of the silver flowers on "n" substrates (a), and "s" substrates (b). FT amplitude patterns of areas 1(c) and 2 (d). Vectors $\mathbf{k}_1$ and $\mathbf{k}_2$ are the corresponding propagation wavevectors of structures in areas 1 and 2. (e) A plot of the FT amplitude along *Y*-direction for the two areas. Overtones of the $\mathbf{k}_2$ wavevector are also marked.

2.2 Methodology of the SERS Measurements

Rhodamine-6G solution of 10^{-3} M concentration was prepared by dilution of 50.3 mg of R6G in 100 ml of deionized (DI) water. Solutions of progressively lower concentrations, ranging from 10^{-4} M to 10^{-7} M, were obtained by four consecutive steps of dilution of the starting 10^{-3} M solution. Where suitable, we will also refer to the solutions by their dilution order (DO), equal to the number of dilution steps. Thus, the molar concentration *C* of the solution is related to DO by the equation:

$$C = 10^{-(3+DO)}. \quad (2)$$

Two substrate samples, one of each series – "s" and "n", were immersed for 1 hour in solutions of all available R6G concentrations. After that the substrates were rinsed with DI water and dried in dark atmosphere at room temperature for 12 hours. The Raman measurements on the as treated substrates were performed on a micro-Raman spectrometer LabRAM HR800 at room temperature with a He-Ne laser (632.8 nm) as an excitation source. A ×50 objective was used both to focus the incident laser beam on a spot of diameter around 5 μm, and to collect the backward scattered light. Since pure R6G is a weak Raman scatterer, reference spectra from R6G solutions were recorded from a liquid cell placed in a retroreflector compartment, which additionally enhances the Raman signal. For a given concentration, Raman spectra were collected from two areas on each type of substrate – on the silver flowers and on the aluminum surface between them. According to the SEM images (see Figure 1) the focused laser spot on the silver flowers illuminates the lateral edges of 10–15 silver sheets. For each substrate, treated in R6G, spectra were collected from at least three randomly chosen silver flowers and three random spots on the bare aluminum surface.

In order to quantify the SERS properties of the substrates, we calculated the normalized intensity $I(\nu)$, associated with the ν-th R6G vibrational mode, as:

$$I(\nu) = S(\nu)/(CP_L), \quad (3)$$

where $S(\nu)$ is the integrated signal obtained by a Lorentzian fit of the corresponding band in the Raman spectrum of the bulk solution or of the substrate treated with that solution, P_L is the excitation laser power, and *C* is the R6G concentration in the solution. The analytic SERS enhancement factor for a specific Raman mode ν was defined according to Reference [40] (eq. 6):

$$EF(\nu) = I_{SERS}(\nu)/I_{sol}(\nu), \quad (4)$$

where $I_{sol}(\nu)$ and $I_{SERS}(\nu)$ are the normalized mode intensities recorded in the bulk of a referent solution and from the silver flower, respectively.

Preprints (www.preprints.org) | NOT PEER-REVIEWED | Posted: 28 October 2021 doi:10.20944/preprints202110.0432.v1

3. Results and Discussion

Figure 2 shows a representative Raman spectrum taken from the bulk of the starting 10^{-3}M solution. The most intense vibrational modes of R6G are easily identifiable and their frequencies are marked on the figure. The SERS properties of the substrates are clearly manifested in Figure 3, where the spectrum of the bulk 10^{-3}M solution (#6) is compared to the spectra 1–5 from silver flowers on "n" substrates treated in R6G solutions of progressively decreasing concentration. The spectra are represented on the same intensity scale and are shifted vertically for clarity. Obviously, the detected Raman signal in spectra 1–5 decreases monotonously with the decrease of the concentration of R6G solution. All R6G vibrational modes are clearly resolved in spectra 1–4, except in spectrum 5, corresponding to smallest R6G concentration, where the spectral lines are masked to a large extent by the spectral noise. Qualitatively similar results have been established for the substrates of the "s" series.

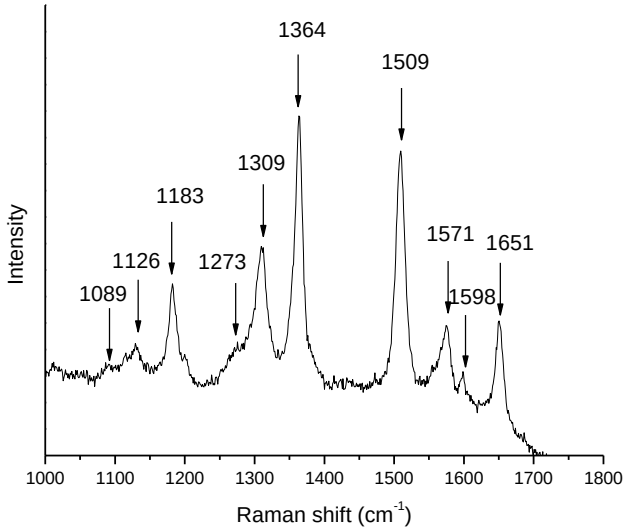

Figure 2. Raman spectrum of 10^{-3}M R6G solution.

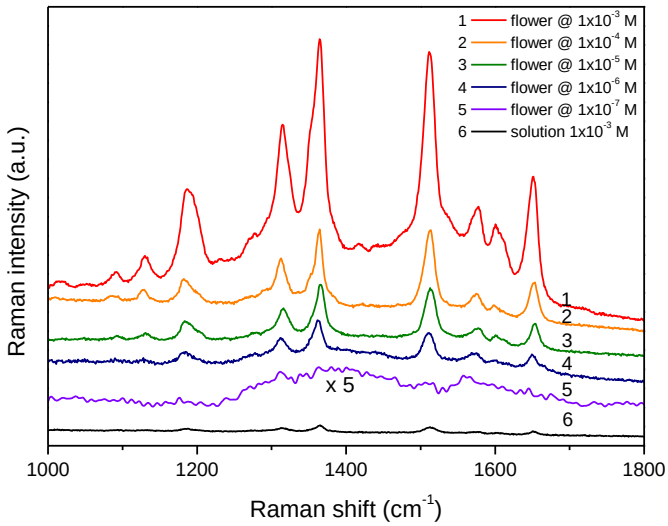

Figure 3. Spectra from silver roses, treated in R6G solutions of different concentration (1–5). Spectrum #6 is taken from the bulk of the 10^{-3}M R6G solution. Spectra correspond to the raw Raman signal and are not normalized to the the solution concentration.

SERS EF for different R6G vibrational modes, calculated according to Equations (3) and (4) for all concentrations, are listed in Table 1. In order to obtain stable fits, the intensity of the R6G spectral lines for samples, treated in the most diluted 10^{-7}M solution,

Preprints (www.preprints.org) | NOT PEER-REVIEWED | Posted: 28 October 2021 doi:10.20944/preprints202110.0432.v1

were estimated by deconvolution of Lorentzian profiles with spectral positions and widths *fixed* to the corresponding values obtained for the 10^{-6}M solution. The last row of the table lists the corresponding spectrum-average enhancement factor (SAEF) defined as $\mathrm{SAEF} = \sum_\nu I_{\mathrm{SERS}}(\nu)/\sum_\nu I_{\mathrm{sol}}(\nu)$, where the sum runs over all detected vibrational modes. Each entry in the table is a statistical average calculated on a sample of at least three randomly chosen silver flowers.

Figure 4 (a) represents the concentration dependence of SAEF. For both types of samples the SERS enhancement systematically increases at low concentrations, reaching optimum values of $\approx 10^5$ for samples treated in 10^{-6}–10^{-7} M R6G solutions. Figure 4 (b) shows the spectral distribution of the EF over different R6G modes. Again, the two types of samples give qualitatively similar results, showing a maximum at low wavenumbers, a pronounced dip for the mode at 1126 cm^{-1} followed by gradual increase for the modes around ≈1300 and 1600 cm^{-1}.

Table 1. The SERS EF for the silver flowers for different R6G modes as a function of the dilution order of the R6G solution. The corresponding spectrum-averaged enhancement factors (SAEF) are shown on the last row. The left and the right columns for each concentration correspond to the "n" and "s" flowers, respectively.

Mode frequency (cm^{-1})	Dilution order									
	0		1		2		3		4	
	EF (×10^2)		EF (×10^3)		EF (×10^3)		EF (×10^4)		EF (×10^5)	
1089	1.6	7.4	1.1	34	5.9	26	21	27	1.3	8.2
1126	0.6	1.5	0.3	0.4	1.5	0.4	1.0	0.4	0.07	0.6
1183	6.4	6.3	1.1	5.3	9.7	2.2	6.4	0.5	0.07	0.8
1273	5.9	5.8	0.2	2.8	1.3	2.5	3.6	3.0	0.29	2.7
1309	3.2	3.3	0.9	4.6	5.9	3.6	7.7	3.9	0.25	0.9
1364	5.5	4.7	1.2	5.7	10	6.4	13	2.3	0.50	1.6
1509	5.9	5.2	1.5	3.6	12	4.8	11	1.6	0.29	0.3
1571	4.2	3.6	0.6	2.5	7.1	2.9	9.9	3.3	0.32	1.7
1598	1.8	1.2	0.3	2.2	2.5	2.1	8.1	3.1	0.32	0.7
1651	4.3	4.3	1.3	3.2	7.8	4.0	9.4	1.8	0.26	0.8
SAEF	**4.0×10^2**	**4.1×10^2**	**8.6×10^2**	**3.2×10^3**	**7.1×10^3**	**4.0×10^3**	**8.3×10^4**	**2.5×10^4**	**3.0×10^4**	**1.1×10^5**

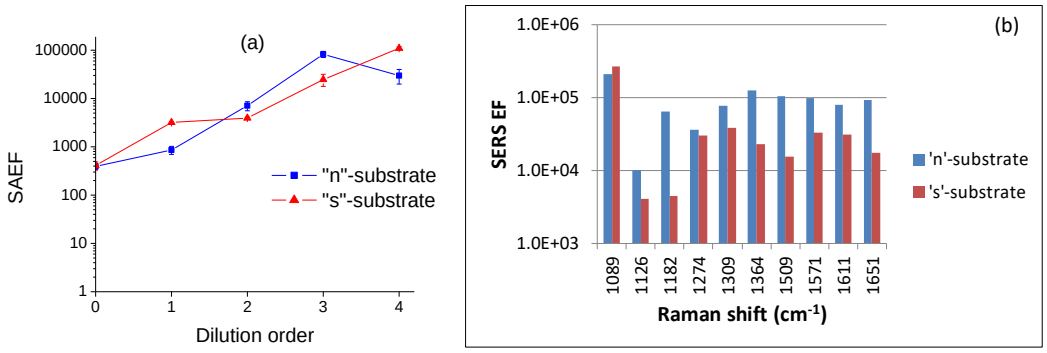

Figure 4. (a) Spectrum-averaged enhancement factor (SAEF) for "n"- and "s"-substrates treated with R6G solutions of different concentrations. (b) SERS enhancement factors for different R6G modes on silver flowers treated in a 10^{-6}M solution.

The concentration dependence of SERS EF is a phenomenon found for different types of substrates and a wide range of analytes [41,42]. Typically, SERS is less effective for higher concentration due to the saturation of adsorption of the analyte molecules on the substrate. Respectively, optimal EF is obtained at smaller concentrations, when monomolecular layer is formed on the substrate [41]. In that case the most favorable

Preprints (www.preprints.org) | NOT PEER-REVIEWED | Posted: 28 October 2021 doi:10.20944/preprints202110.0432.v1

conditions are met for both the chemical and the electrodynamic enhancement mechanisms, since adsorbed molecules are in a direct chemical contact with the substrate, and at the same time sense the highest local electric field.

As already discussed (see Figure 1), the two types of silver flowers consist of self-organized quasiperiodic arrays, which could be modeled as rectangular gratings of vertical sheets of a thickness b, separated by grooves (voids) of a width $a = \Lambda - b$, where Λ is the grating period, as illustrated in Figure 5 (a). The depth h of the grooves is of the order of 2–3 μm, i.e. exceeds several times the grating period. Therefore, this structure is equivalent to a system of coupled nanocavity resonators, which transmits the SP waves along the inner silver-air interface in depth of the grooves (see Figure 5 (a)). The resonant frequencies of the cavity are approximately given by the standing wave condition for an open-end resonator:

$$2h = (m + \phi/(2\pi))\lambda_{SP}, \tag{4}$$

where λ_{SP} is the frequency-dependent SP wavelength, and ϕ is the phaseshift of the wave reflected from the bottom of the grooves, and m is the number of wave nodes.

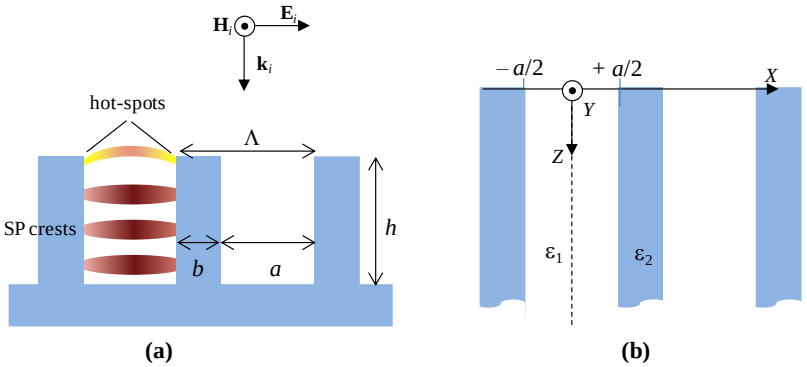

Figure 5. (a) Schematic model of a rectangular metallic grid. A TM polarized wave is incident normally on the grating, along the wavevector $\mathbf{k}_i$. The electric field $\mathbf{E}_i$ of the wave is perpendicular to the metallic sheets (i.e. along the propagation direction of the grid); the magnetic field $\mathbf{H}_i$ is parallel to the edges of the grooves. The ovals represent schematically the crests of the standing SP wave inside the air cavity. The yellow arc marks the position of the SERS hot-spots near the edges of the metallic grooves. (b) Choice of a coordinate system for description of the SP waves guided along the dielectric cavities.

Theoretical models of SP excitations in single nanocavities [43,44] and in periodic rectangular gratings [45,46] suggest that the strongest electrodynamic enhancement takes place near the parallel edges of the metallic sheets, which could act as effective SERS hot spots [47]. In contrast to hot-spots found in nanoparticle based SERS substrates, which are essentially point-like (0D) objects, the hot-spots in metallic gratings have linear (1D) character, and can accommodate a larger number of adsorbed molecules. The estimated electrodynamic enhancement of the electric field intensity $|E/E_0|$ near the opening of a nanocavity resonator is of order of 10^1 [43,47]. Since SERS intensity scales as $|E/E_0|^4$, purely electrodynamic EFs of order 10^4 are achievable near the grooves edges. However, for SP resonances transmitted in depth of the grooves, electric field enhancement takes places also over the inner metal-dielectric interface, near the crests of the standing SP wave (see Figure 5 (a)).. Numerical simulations evidence that molecules adsorbed deeply in the grating grooves also have significant contribution to the SERS signal, raising the average EF up to an order of magnitude [47]. Therefore, the expected SERS EFs for silver gratings with sufficiently deep groves may reach values of 10^5, which corroborates the estimated maximum EFs in our experiments.

The SP in a metallic grating is excited by an electromagnetic wave of TM polarization, i.e. with a magnetic field parallel to the groove edges, and an electric field having component parallel to the grating propagation vector (see Figure 5 (a)). As seen in Figure 1, any single silver flower is composed of several arrays whose propagation vectors span

 doi:10.20944/preprints202110.0432.v1

different directions. Therefore, irrespectively of the polarization of the laser excitation, there are arrays, coupled to the electric field of the incident wave.

The availability of a large number of groove edges illuminated by the laser excitation implies that the EM enhancement in the silver flowers proceeds mainly through the formation of linear hot-spots. However, it is important also to assess the possible contribution of the molecules adsorbed in-depth of the grooves to the overall Raman signal. By following the procedure, described in Appendix A, we established that for the typical geometric parameters of the grating, the SP dispersion inside the grooves, for frequencies in the optical range, is almost photon-like (see Figure A1). In the Raman spectrum window the SP wavelength λ_{SP} is by 6–7% smaller than the corresponding wavelength λ_0 in the free space. The corresponding effective SP refraction index $n_{SP} = \lambda_0/\lambda_{SP}$ takes values 1.06 and 1.07 for "n"- and "s"-flowers, respectively (see Table A1). According to Equation (5), for a typical groove depth of 2–3 μm and a phaseshift $\phi \approx 26°$ (0.45 rad) at $\lambda_0 = 633–700$ nm, SP resonances between 6-th and 9-th order could be expected in the Stokes part of the Raman spectrum. Therefore, the presence of several SP crests in depth of the grooves suggests that the SERS signal is recorded not only from the edge hot-spots but also over a large part of the surface of the silver sheets.

4. Summary and Conclusions

In summary, we report the preparation and characterization of SERS substrates based on silver flowerlike particles of high surface-to-volume ratio. The nanoscale morphology of the silver flowers is dominated by self-assembled arrays of vertically standing metallic sheets of subwavelength periodicity. The recorded SERS enhancement factors on the silver flowers reach highest values of $\propto 10^5$ at lowest analyte concentrations of 10^{-6}–10^{-7}M.

The major contribution to the SERS enhancement stems from the groove edges, which act as effective "hot-lines". The periodic nanosheet arrays, however, form coupled resonator cavities, which guide the surface plasmon waves in depth of the silver flowers, providing additional electric filed enhancement over large effective area.

The work opens prospects for further research, like optimization of the preparation conditions for obtaining predefined morphology of the nanosheet arrays within silver flowers, testing the substrates against different analytes, and investigation of the possibility for multiple usage/washability of the substrates. Electronic beam lithography allows for selective "seeding" of silver flowers in predefined positions, including in ordered patterns [38], which infers for promising on-chip applications of this type or SERS substrates in biosensing and in medical analysis.

Author Contributions: Conceptualization, all authors, substrate fabrication and SEM imaging, G.G.T. and S.C.R., Raman measurements, N.D.T. M.V.A. and V.G.I., calculations, V.G.I., data analysis, visualization, and writing —original draft preparation, G.G.T. and V.G.I., writing—review and editing, N.D.T., S.C.R. M.V.A. and A.V.L., project administration and funding acquisition, A.V.L. and V.G.I. All authors have read and agreed to the published version of the manuscript.

Funding: This research was funded by the Bulgarian-Russian bilateral project through the contracts KP-06-15/27.09.2019 Russia with the Bulgarian National Fund of Scientific Research (G.G.T, N.D.T., S.C.R., V.G.I.) and 19-52-18008 Bulg of RFBR (A.V.L.).

Informed Consent Statement: Not applicable.

Data Availability Statement: Publicly available datasets from Refractive Index Database were analyzed in this study. This data can be found here: https://refractiveindex.info. The source is cited in the References section.

Acknowledgments: Facilities of the National Center of Mechatronics and Clean Technologies were used in this research through the contract BG05M2OP001-1.001-0008 (N.D.T., M.V.A, V.G.I.).

Conflicts of Interest: The authors declare no conflict of interest. The funders had no role in the design of the study; in the collection, analyses, or interpretation of data; in the writing of the manuscript, or in the decision to publish the results.

Preprints (www.preprints.org) | NOT PEER-REVIEWED | Posted: 28 October 2021 doi:10.20944/preprints202110.0432.v1

Appendix A

In this appendix we formulate the necessary approximations and derive the dispersion relations for the SP modes, transmitted into the depth of a metallic grating with deep rectangular grooves. The coordinate origin is placed midway between the upper edges of two neighboring metallic slabs, as shown in Figure 5 (b). The permittivity of the dielectric medium above the metal is ε_1 and the permittivity of the metal is ε_2. We will neglect the energy losses in the metal and in the dielectric, assuming that ε_1 and ε_2 are real.

The SP is excited by a TM polarized plane electromagnetic wave of angular frequency ω and wavelength in free space $\lambda_0 = 2\pi c/\omega$, incident normally onto the grating, i.e. in Z-direction. The electric field $\mathbf{E}_i$ and the magnetic field $\mathbf{H}_i$ the incident wave are parallel to the X- and Y-directionsis, respectively. Since the X-component of the wavevector of the incident wave is zero, the field of excited SP waves could be expanded in harmonic components with propagation vector along X, multiple of $2\pi/\Lambda$. Therefore, the electric and magnetic field of the SP wave satisfy the periodic boundary conditions $\mathbf{E}(x) = \mathbf{E}(x + \Lambda)$ and $\mathbf{H}(x) = \mathbf{H}(x + \Lambda)$, respectively. We assume that $\omega < \omega_p$ (the plasma frequency of the metal), which means that $\varepsilon_2 < 0$ and the electromagnetic field falls off exponentially inside the metallic slabs.

Since in our case $\Lambda < \lambda_0$ we will follow the approach in Reference [44] for calculating the dispersion relation in a single metal-insulator-metal (MIM) cavity of a subwavelength width a and a much bigger depth h. Therefore, the grating will be modeled as a periodic MIMIM… array of infinite waveguides, which transmit SP waves of a wavevector q along the Z-direction.

Due to the periodic boundary conditions, we consider filed behavior only in the "elementary cell" $x \in [-a/2\,;\Lambda - a/2]$, which includes the $[-a/2\,;+a/2]$ dielectric cavity and the neighboring metallic sheet to the right. The non-zero components of the magnetic field $\mathbf{H}$ and the electric field $\mathbf{E}$ in the dielectric (labeled with index 1), and in the metal (labeled with index 2), which satisfy the Maxwell equations, and are consistent with the polarization of the incident wave, have the form:

$$H_{1y} = F_1 \cosh(\eta_1 x)\, e^{i(qz-\omega t)};\;\; H_{2y} = F_2 \cosh\big(\eta_2 (x - \Lambda/2)\big)\, e^{i(qz-\omega t)}; \tag{A1}$$

$$E_{1z} = \frac{i\eta_1 F_1}{\omega \varepsilon_1 \varepsilon_0} \sinh(\eta_1 x)\, e^{i(qz-\omega t)};\;\; E_{2z} = \frac{i\eta_2 F_2}{\omega \varepsilon_2 \varepsilon_0} \sinh\big(\eta_2 (x - \Lambda/2)\big)\, e^{i(qz-\omega t)}; \tag{A2}$$

$$E_{1x} = \frac{qF_1}{\omega \varepsilon_1 \varepsilon_0} \cosh(\eta_1 x)\, e^{i(qz-\omega t)};\;\; E_{2x} = \frac{qF_2}{\omega \varepsilon_2 \varepsilon_0} \cosh\big(\eta_2 (x - \Lambda/2)\big)\, e^{i(qz-\omega t)}. \tag{A3}$$

Here F_1 and F_2 are the complex amplitudes of the magnetic field in the dielectric and in the metal, respectively, $\eta_1 = \sqrt{q^2 - (\omega/c)^2 \varepsilon_1}$ and $\eta_2 = \sqrt{q^2 - (\omega/c)^2 \varepsilon_2}$ are the corresponding exponential-decay constants. After applying the field boundary conditions:

$$H_{1y} = H_{2y};\; E_{1z} = E_{2z};\; \varepsilon_1 E_{1x} = \varepsilon_2 E_{2x} \tag{A4}$$

at the metal-dielectric interface at $x = +a/2$, we derive the dispersion relation for the SP modes:

$$\frac{\eta_1}{\varepsilon_1} \tanh(\eta_1 a/2) = -\frac{\eta_2}{\varepsilon_2} \tanh(\eta_2 b/2) \tag{A5}$$

Equation (A5) reproduces the result for a single MIM cavity [44] in the limit $b \to \infty$ at finite a. On the other hand, if both $a, b \to \infty$, the classical SP dispersion relation: $q^2 = (\omega/c)^2 \varepsilon_1 \varepsilon_2/(\varepsilon_1 + \varepsilon_2)$ for a single MI interface is obtained.

In what follows, we take $\varepsilon_1 = 1$ for the air, while ε_2 is the frequency-dependent electric permittivity of silver at $\omega < \omega_p$, taken from Reference [48] and available in numeric form from the Refractive Index Database [49]. The geometric parameters of the model grids, representing the two types of silver flowers, are summarized in Table A1. The lower panel of Figure 1 shows the calculated dependence of the SP wavelength $\lambda_{SP} = 2\pi/q$ on the wavelength $\lambda_0 = 2\pi c/\omega$ in the free space at $\lambda_0 > \Lambda$. The upper panel of

Preprints (www.preprints.org) | NOT PEER-REVIEWED | Posted: 28 October 2021 doi:10.20944/preprints202110.0432.v1

the figure presents the wavelength dependence of the effective SP refraction index $n_{SP} = \lambda_0/\lambda_{SP}$.

Table A1. Model grid parameters for the two types of silver flowers. The last row represents the surface-plasmon effective refraction index n_{SP}, calculated at the wavelength $\lambda_0 = 663$ nm of the incident laser wave.

Parameter	"n"-flowers	"s"-flowers
Λ (nm)	580	390
Filing factor F	0.15	0.15
$a = (1-F)\Lambda$ (nm)	493	332
$b = F\Lambda$ (nm)	87	58
n_{SP}(633 nm)	1.060	1.079

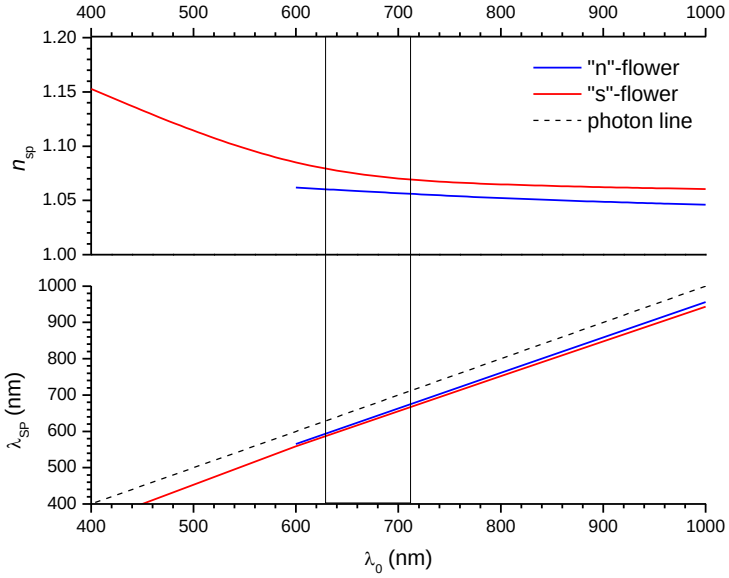

Figure A1. Lower panel: Dependence of the SP wavelength λ_{SP} (lower panel) and the effective SP refraction index n_{SP} on the free-space wavelength λ_0. Only values $\lambda_0 > \Lambda$ are presented. The Raman spectrum window is marked with vertical lines.

References

1. Campion, A.; Kambhampati, P. Surface-Enhanced Raman Scattering. *Chem. Soc. Rev.* **1998**, *27* (4), 241–250.
2. Tian, Z. Q. Surface-Enhanced Raman Spectroscopy: Advancements and Applications. *J. Raman Spectrosc.* **2005**, *36* (6–7), 466–470.
3. Cialla, D.; Marz, A.; Bohme, R.; Theil, F.; Weber, K.; Schmitt, M.; Popp, J. Surface-Enhanced Raman Spectroscopy (SERS): Progress and Trends. *Anal. Bioanal. Chem.* **2012**, *403* (1), 27–54.
4. Sharma, B.; Frontiera, R. R.; Henry, A. I.; Ringe, E.; Van Duyne, R. P. SERS: Materials, Applications, and the Future. *Mater. Today* **2012**, *15* (1–2), 16–25.
5. Zhang, W.; Yeo, B. S.; Schmid, T.; Zenobi, R. Single Molecule Tip-Enhanced Raman Spectroscopy with Silver Tips. *J Phys Chem C* **2007**, *111*, 1733–1738.
6. Zrimsek, A. B. Single-Molecule Chemistry with Surface-and Tip-Enhanced Raman Spectroscopy. *Chem Rev* **2016**, *117*, 7583–7613.
7. Zong, C.; Premasiri, R.; Lin, H.; Huang, Y.; Zhang, C.; Yang, C.; Ren, B.; Ziegler, L. D.; Cheng, J.-X. Plasmon-Enhanced Stimulated Raman Scattering Microscopy with Single-Molecule Detection Sensitivity. *Nat. Commun.* **2019**, *10* (1), 5318.

8. Chen, Y.; Premasiri, W.; Ziegler, L. Surface Enhanced Raman Spectroscopy of Chlamydia Trachomatis and Neisseria Gonorrhoeae for Diagnostics, and Extra-Cellular Metabolomics and Biochemical Monitoring. *Sci Rep* **2018**, *8*, 5163.
9. Felten, J. Vibrational Spectroscopic Image Analysis of Biological Material Using Multivariate Curve Resolution–Alternating Least Squares (MCR-ALS). *Nat Protoc* **2015**, *10*. https://doi.org/10.1038/nprot.2015.008.
10. Zong, C. Surface-Enhanced Raman Spectroscopy for Bioanalysis: Reliability and Challenges. *Chem Rev* **2018**, *118*.
11. Kim, N.; Thomas, M. R.; Bergholt, M. S.; Pence, I. J.; Seong, H.; Charchar, P.; Todorova, N.; Nagelkerke, A.; Belessiotis-Richards, A.; Payne, D. J.; Gelmi, A.; Yarovsky, I.; Stevens, M. M. Surface Enhanced Raman Scattering Artificial Nose for High Dimensionality Fingerprinting. *Nat. Commun.* **2020**, *11* (1), 207.
12. Kambhampati, P.; Child, C. M.; Foster, M. C.; Campion, A. On the Chemical Mechanism of Surface Enhanced Raman Scattering: Experiment and Theory. *J. Chem. Phys.* **1998**, *108* (12), 5013–5026.
13. Schatz, G. C.; Young, M. A.; Duyne, R. P. Electromagnetic Mechanism of SERS. In *Surface-Enhanced Raman Scattering*; Kneipp, K., Moskovits, M., Kneipp, H., Eds.; Topics in Applied Physics; Springer Berlin Heidelberg, 2006; Vol. 103, pp 19–45.
14. West, P. R.; Ishii, S.; Naik, G. V.; Emani, N. K.; Shalaev, V. M.; Boltasseva, A. Searching for Better Plasmonic Materials. *Laser Photonics Rev.* **2010**, *4* (6), 795–808.
15. Etchegoin, P.; Cohen, L. F.; Hartigan, H.; Brown, R. J. C.; Milton, M. J. T.; Gallop, J. C. Electromagnetic Contribution to Surface Enhanced Raman Scattering Revisited. *J. Chem. Phys.* **2003**, *119* (10), 5281–5289.
16. McRae, D. M.; Lagugné-Labarthet, F. In Search of the Hot Spot. *Nat. Nanotechnol.* **2019**, *14* (10), 922–923.
17. Pettinger, B.; Picardi, G.; Schuster, R.; Ertl, G. Surface-Enhanced and STM-Tip-Enhanced Raman Spectroscopy at Metal Surfaces. *Single Mol.* **2002**, *3* (5–6), 285–294..
18. Steidtner, J.; Pettinger, B. Tip-Enhanced Raman Spectroscopy and Microscopy on Single Dye Molecules with 15 Nm Resolution. *Phys. Rev. Lett.* **2008**, *100* (23), 236101.
19. Liu, Y. C.; Yu, C. C.; Sheu, S. F. Low Concentration Rhodamine 6G Observed by Surface-Enhanced Raman Scattering on Optimally Electrochemically Roughened Silver Substrates. *J. Mater. Chem.* **2006**, *16* (35), 3546–3551.
20. Yang, K. H.; Liu, Y. C.; Yu, C. C. Simple Strategy To Improve Surface-Enhanced Raman Scattering Based on Electrochemically Prepared Roughened Silver Substrates. *Langmuir* **2010**, *26* (13), 11512–11517.
21. Surface-Enhanced Raman Scattering Investigations on Silver Nanoparticles Deposited on Alumina and Titania Nanotubes: Influence of the Substrate Material on Surface-Enhanced Raman Scattering Activity of Ag Nanoparticles : Surface-Enhanced Raman Scattering Investigations. *J. Raman Spectrosc.* **2012**, *43* (10), 1360-1366.
22. In Situ Controlled Growth of Well-Dispersed Gold Nanoparticles in TiO2 Nanotube Arrays as Recyclable Substrates for Surface-Enhanced Raman Scattering. *Dalton Trans.* **2012**, *41* (3), 1020.
23. Surface-Enhanced Raman Scattering (SERS) Activity of Ag, Au and Cu Nanoclusters on TiO2-Nanotubes/Ti Substrate. *Appl. Surf. Sci.* **2011**, *257* (19), 8182.
24. Raman Enhancement of Rhodamine Adsorbed on Ag Nanoparticles Self-Assembled into Nanowire-like Arrays. *Nanoscale Res. Lett.* **2011**, *6* (1), 629.
25. Ritacco, T.; Ricciardi, L.; Deda, M. L.; Giocondo, M. Controlling the Optical Creation of Gold Nanoparticles in a PVA Matrix by Direct Laser Writing. *J. Eur. Opt. Soc. Rapid Publ.* **2016**, *11*, 16008.
26. Ivanov, V. G.; Todorov, N. D.; Petrov, L. S.; Ritacco, T.; Giocondo, M.; Vlakhov, E. S. Strong Surface Enhanced Raman Scattering from Gold Nanoarrays Obtained by Direct Laser Writing. *J. Phys. Conf. Ser.* **2016**, *764*, 012023.
27. Michaels, A. M.; Nirmal, M.; Brus, L. E. Surface Enhanced Raman Spectroscopy of Individual Rhodamine 6G Molecules on Large Ag Nanocrystals. *J. Am. Chem. Soc.* **1999**, *121* (43), 9932–9939.
28. Chen, H.; Simon, F.; Eychmuller, A. Large-Scale Synthesis of Micrometer-Sized Silver Nanosheets. *J. Phys. Chem. C* **2010**, *114* (10), 4495–4501.

29. Jie, Z.; Zenghe, Y.; Tiancheng, G.; Yunfei, L.; Dapeng, W.; Yong, Z. Graphene/Ag Nanoholes Composites for Quantitative Surface-Enhanced Raman Scattering. *Opt. Express* **2018**, *26* (17), 22432.
30. Vigderman, L.; Zubarev, E. R. Starfruit-Shaped Gold Nanorods and Nanowires: Synthesis and SERS Characterization. *Langmuir* **2012**, *28* (24), 9034–9040.
31. Lee, M.-K.; Seo, J.; Jin Cho, S.; Jo, Y.; Kim, S.; Youngjong Kang, H. L. Novel 3D Arrays of Gold Nanostructures on Suspended Platinum-Coated Carbon Nanotubes as Surface-Enhanced Raman Scattering Substrates. *Mater. Lett.* **2012**, *81*, 9–12.
32. Ding, S.-Y.; Yi, J.; Li, J.-F.; Ren, B.; Wu, D.-Y.; Panneerselvam, R.; Tian, Z.-Q. Nanostructure-Based Plasmon-Enhanced Raman Spectroscopy for Surface Analysis of Materials. *Nat. Rev. Mater.* **2016**, *1* (6), 16021.
33. Nafie, L. A. Recent Advances in Linear and Nonlinear Raman Spectroscopy. Part VI: Recent Advances in Linear and Nonlinear Raman Spectroscopy. Part VI. *J. Raman Spectrosc.* **2012**, *43* (12), 1845–1863.
34. Chen, J. N.; Martensson, T.; Dick, K. A.; Deppert, K.; Xu, H. Q.; Samuelson, L.; Xu, H. X. Surface-Enhanced Raman Scattering of Rhodamine 6G on Nanowire Arrays Decorated with Gold Nanoparticles. *Nanotechnology* **2008**, *19* (27).
35. Nasrollahzadeh, M.; Issaabadi, Z.; Sajjadi, M.; Sajadi, S. M.; Atarod, M. Types of Nanostructures. In *Interface Science and Technology*; Elsevier, 2019; Vol. 28, pp 29–80.
36. Shende, P.; Kasture, P.; Gaud, R. S. Nanoflowers: The Future Trend of Nanotechnology for Multi-Applications. *Artif. Cells Nanomedicine Biotechnol.* **2018**, *46* (sup1), 413–422.
37. Zhang, G.; Deng, C.; Shi, H.; Zou, B.; Li, Y.; Liu, T.; Wang, W. ZnO/Ag Composite Nanoflowers as Substrates for Surface-Enhanced Raman Scattering. *Appl. Surf. Sci.* **2017**, *402*, 154–160.
38. Tsutsumanova, G.; Lyutov, L.; Tzonev, A.; Russev, S. Ordering of Silver Flowerlike Nanosheet Structures on an Aluminium Substrate. *Mater. Lett.* **2008**, *62* (20), 3588–3590.
39. He, Y.; Wu, X. F.; Lu, G. W.; Shi, G. Q. Fabrication of Two-Dimensional Staggered Silver Nanosheets on an Aluminium Foil. *Nanotechnology* **2005**, *16* (6), 791–796.
40. Le Ru, E. C.; Etchegoin, P. G. Quantifying SERS Enhancements. *MRS Bull.* **2013**, *38* (8), 631–640.
41. Ojha, A. K.; Donfack, P.; Materny, A. Complex Concentration Dependence of SERS and UV-Vis Absorption of Glycine/Ag-Substrates Because of Glycine-Mediated Ag-Nanostructure Modifications: Complex Concentration Dependence of SERS and UV-Vis Absorption of Glycine/Ag-Substrates. *J. Raman Spectrosc.* **2012**, *43* (9), 1183–1190.
42. Gamberini, M. C.; Mary, Y. S.; Mary, Y. S.; Krátký, M.; Vinsova, J.; Baraldi, C. Spectroscopic Investigations, Concentration Dependent SERS, and Molecular Docking Studies of a Benzoic Acid Derivative. *Spectrochim. Acta. A. Mol. Biomol. Spectrosc.* **2021**, *248*, 119265.
43. Miyazaki, H. T.; Kurokawa, Y. Controlled Plasmon Resonance in Closed Metal/Insulator/Metal Nanocavities. *Appl. Phys. Lett.* **2006**, *89* (21), 211126.
44. Kurokawa, Y.; Miyazaki, H. T. Metal-Insulator-Metal Plasmon Nanocavities: Analysis of Optical Properties. *Phys. Rev. B* **2007**, *75* (3), 035411.
45. Xu, S.; Su, H.; Qin, K.; Xie, Y.; Wang, Q.; Zhang, X.; Lu, Y.; Zhu, Y. SERS Application of Propagating Surface Plasmon Modes in 1D Metallic Gratings; Li, L., Hong, M., Jiang, L., Eds.; Beijing, China, 2015; p 96730T.
46. Yaremchuk, I.; Petrovska, H.; Karelko, I.; Fitio, V.; Bobitski, Y. Optimization of the Grating-Based Structures for the Efficient SERS Substrates. In *2017 IEEE 37th International Conference on Electronics and Nanotechnology (ELNANO)*; IEEE: Kyiv, Ukraine, 2017; pp 119–123.
47. Mattiucci, N.; D'Aguanno, G.; Everitt, H. O.; Foreman, J. V.; Callahan, J. M.; Buncick, M. C.; Bloemer, M. J. Ultraviolet Surface-Enhanced Raman Scattering at the Plasmonic Band Edge of a Metallic Grating. *Opt. Express* **2012**, *20* (2), 1868.

 doi:10.20944/preprints202110.0432.v1

48. Johnson, P. B.; Christy, R. W. Optical Constants of the Noble Metals. *Phys. Rev. B* **1972**, *6* (12), 4370–4379.
49. Polyanskiy, M. N. Refractive Index Database, https://refractiveindex.info. Accessed on 2021-10-15.